

Synergetic bifunctional Cu-In alloy interface enables Ah-level Zn metal pouch cells

Received: 7 February 2024

Accepted: 21 October 2024

Published online: 01 November 2024

 Check for updates


Minghao Zhang¹, Chenxi Sun¹, Guan hong Chen¹, Yuanhong Kang¹, Zeheng Lv¹, Jin Yang¹, Siyang Li¹, Pengxiang Lin¹, Rong Tang¹, Zhipeng Wen², Cheng Chao Li², Jinbao Zhao^{1,3}  & Yang Yang^{1,3} 

Rechargeable aqueous zinc-metal batteries, considered as the possible post-lithium-ion battery technology for large-scale energy storage, face severe challenges such as dendrite growth and hydrogen evolution side reaction (HER) on Zn negative electrode. Herein, a three-dimensional Cu-In alloy interface is developed through a facile potential co-replacement route to realize uniform Zn nucleation and HER anticatalytic effect simultaneously. Both theoretical calculations and experimental results demonstrate that this bifunctional Cu-In alloy interface inherits the merits of low Zn-nucleation overpotential and high HER overpotential from individual copper and indium constituents, respectively. Moreover, the dynamical self-reconstruction during cycling leads to an HER-anticatalytic and zincophilic gradient hierarchical structure, enabling highly reversible Zn chemistry with dendrite-free Zn (002) deposition and inhibited HER. Moreover, the improved interface stability featured by negligible pH fluctuations in the diffusion layer and suppressed by-product formation is evidenced by in-situ scanning probe technology, Raman spectroscopy, and electrochemical gas chromatography. Consequently, the lifespan of the CuIn@Zn symmetric cell is extended to more than one year with a voltage hysteresis of 6 mV. Importantly, the CuIn@Zn negative electrode is also successfully coupled with high-loading iodine positive electrode to fabricate Ah-level (1.1 Ah) laminated pouch cell, which exhibits a capacity retention of 67.9% after 1700 cycles.

Since the invention and commercialization of Lithium-ion batteries (LIBs) decades ago, they have evolved into the primary energy source for electric vehicles, consumer electronics, and grid-scale energy storage¹. However, the escalating dependence on LIBs in these application sectors has also highlighted their deficiency in terms of safety performance, environmental sustainability, and cost driven by the limited reserves of lithium sources^{2,3}. In response to the growing demand for secure and cost-effective energy storage devices, aqueous zinc-metal batteries (AZMBs) have emerged as highly promising

alternatives to LIBs⁴⁻⁶. This is attributed to their non-flammable aqueous electrolyte and water-compatible metallic zinc negative electrode, which possesses a high specific capacity of 820 mAh g⁻¹ and low redox potential of -0.76 V (vs. standard hydrogen electrode (SHE))⁷⁻¹⁰. However, the irreversible Zn chemistry on the negative electrode side, marked by notorious dendrite growth, parasitic hydrogen evolution side reaction (HER), and the concomitant accumulation of by-products (such as basic zinc sulfate, Zn₄SO₄(OH)₆·xH₂O, ZSH) (Fig. 1a), results in low Zn utilization ratio, increased internal resistance and the risk of

¹State Key Laboratory of Physical Chemistry of Solid Surfaces, College of Chemistry and Chemical Engineering, Xiamen University, Xiamen, P. R. China.

²School of Chemical Engineering and Light Industry, Guangdong University of Technology, Guangzhou, P. R. China. ³State-Province Joint Engineering Laboratory of Power Source Technology for New Energy Vehicle, Xiamen, P. R. China.  e-mail: jbzhao@xmu.edu.cn; yangyang419@xmu.edu.cn

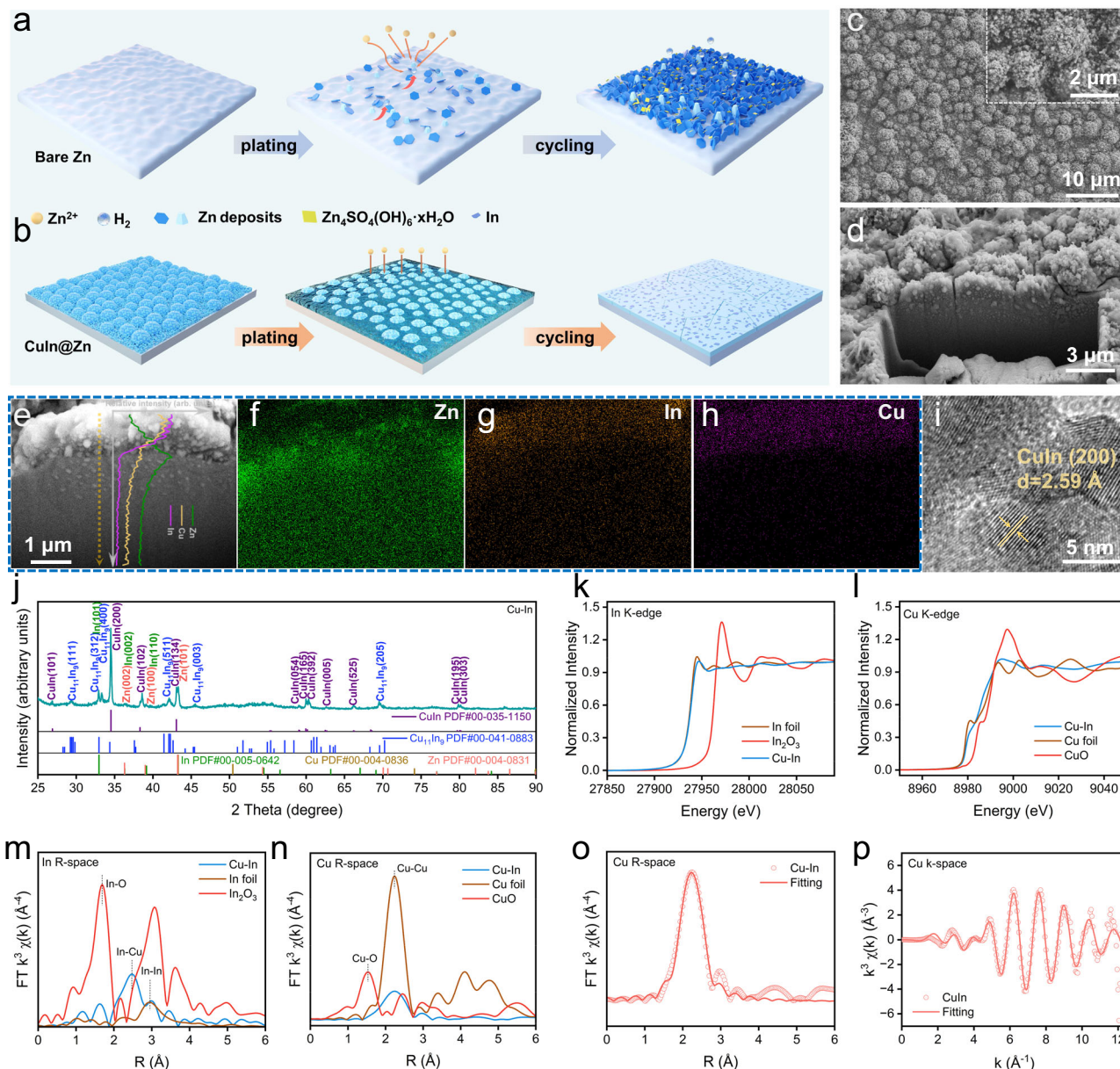


Fig. 1 | Schematic diagram as well as structural and morphological characterizations for CuIn@Zn. Schematic diagram of **a** uncontrolled Zn chemistry on bare Zn and **b** Cu–In alloy layer suppressing the HER and regulating the Zn deposition. **c** SEM images of pristine CuIn@Zn. **d, e** The cross-section SEM images of CuIn@Zn foils (inset is the corresponding EDS line scanning results) and **f–h** the

corresponding distribution of elements of CuIn@Zn. **i** The HRTEM images of Cu–In powder. **j** XRD patterns of pristine Cu–In particles. **k** The normalized XANES spectra of **k** In K-edge and **l** Cu K-edge. Fourier transform (FT) of EXAFS spectra of **m** In K-edge and **n** Cu K-edge in R-space. EXAFS curves fitting of Cu K-edge in **o** R space and **p** k space.

short-circuiting, impeding the further progress of AZMBs in practical applications^{11–13}.

According to the classical heterogeneous nucleation theory, Zn²⁺ ions accept electrons to form Zn embryos at nucleation active sites when the potential reaches a dip^{14,15}. Following instantaneous nucleation, the potential rises to a plateau potential, allowing for the subsequent growth of Zn nuclei¹⁶. Moreover, Zn²⁺ ions exhibit a tendency to gather and deposit in the vicinity of the already formed Zn nuclei due to the deformation of the electric field, further facilitating the continuous growth stage¹⁷. Therefore, Zn nucleation is one of the most essential steps that influence the zinc deposition morphology and induces the formation of dendrites^{6,18,19}. Accordingly, various zincophilic metallic sites (Co, Sn, Cu, Ag, Ni, Bi, Sb)^{20–28}, have been adopted to optimize nucleation due to their relatively large binding energies with Zn atoms. The tuned interfacial interaction between the

substrate and Zn can lower the Zn nucleation barrier, leading to a smaller nucleation overpotential and suppressing dendritic Zn growth^{27,29}. Besides, hydrogen evolution reaction (HER) is also another core issue to exacerbate the reversibility^{30–32}. The conventional single-component zincophilic substrate design, however, faces challenges in simultaneously addressing these issues such as HER and chemical corrosion²⁶. Specifically, the alkaline environment induced by these processes results in the accumulation of ZSH at the interface³³. This weakens the bonding forces between zinc deposits and the substrate, inducing dendrite formation³¹. Meanwhile, the dendrites will extend the exposure area of active zinc, creating more HER sites and exacerbating the deterioration of the Zn negative electrode³⁴. A direct strategy to stabilize the Zn surface is to construct an artificial layer that effectively restrains free water molecules and detrimental anions from reacting with the inner metallic Zn^{35–39}. From a fundamental

perspective, designing a functional interface with both good zincophilicity and a passivated electrocatalytic feature for HER appears to be the ultimate solution for achieving reversible and stable Zn metal negative electrodes^{40–43}. It is also noteworthy that most previously reported advancements for Zn metal full batteries are performed on laboratory-scale coin cells. While there are a few studies reporting Zn metal pouch cells, they often fail to deliver prolonged cycle life (>500 cycles) at a relatively high cell-level energy (>1 Ah). Very recently, Zhi et al.^{44,45} pioneered the development of high volumetric energy density zinc metal pouch cells using vanadium oxides as positive electrodes, paving the way to practical AZMBs. However, developing Ah-level Zn-I pouch cells with satisfactory cycling stability is still a great challenge due to the low Zn utilization induced by HER and corrosion of shuttled polyiodides. Moreover, considering that any minor defect in coin cells can be magnified in a practical pouch cell⁴⁶, the consistency of many reported modification strategies in realistic high-energy Zn metal batteries should be carefully examined.

Herein, a readily accessible three-dimensional (3D) Cu–In alloy heterogeneous interface (CuIn@Zn) is developed to realize uniform Zn nucleation and hydrogen evolution anticatalytic effect simultaneously. The Cu–In alloy inherits the zincophilicity of copper, reducing the Zn nucleation barrier and suppressing dendritic Zn growth. Besides, the alloying of indium improves the HER anticatalytic property (anti-HER) of Cu–In interface, thereby mitigating uncontrolled Zn degradation and resulting in a flat, by-product-free zinc electrodeposited layer with Zn (002) preferential orientation (Fig. 1b). Moreover, the CuIn@Zn is observed to be self-reconstructed during cycling due to the slow oxidation and reduction of indium, leading to a zincophilic and HER-anticatalytic gradient hierarchical structure, thereby maximizing the synergistic regulation. As a result, the Cu–In layer enables the CuIn@Zn|CuIn@Zn symmetric cell stably cycles for more than 1 year at 1 mA cm⁻² for 1 mAh cm⁻². More importantly, the CuIn@Zn||Zn pouch cell can deliver an Ah level capacity (1.1 Ah) for more than 1700 cycles, and steady power for the small electronic device, evidencing its practical potential. Based on the design of a multifunctional interface, this work highlights the indispensability of both zincophilicity and HER kinetics toward highly reversible practical Zn negative electrode.

Results

Structural and morphological characterizations

The Cu–In alloy interface is formed on the surface of metallic Zn through a straightforward potential co-replacement route. As shown in SEM (scanning electron microscope) images of the as-prepared CuIn@Zn electrode (Fig. 1c), the surface is coated with a three-dimensional (3D) spherical interface. Element mappings indicate that Cu, In, and Zn are homogeneously distributed in the layer (Supplementary Fig. 1) and the primary particles of the interface layer (Supplementary Fig. 2), which is consistent with the results of XPS (X-ray photoelectron spectroscopy) (Supplementary Fig. 3). The content of residual zinc in the Cu–In layer is quantified as 10 wt% by inductively coupled plasma optical emission spectrometer (ICP-OES, Supplementary Table 1). Furthermore, to clearly observe the surface structure of CuIn@Zn, focused ion beam machining system (FIB) processing was employed to expose the cross-section of the Cu–In alloy interface. As depicted in Fig. 1d, the Cu–In layer with a thickness of a few microns integrates tightly with the Zn substrate without any particle shedding. Meanwhile, elemental analysis reveals that the Cu and In elements were predominantly distributed at the top region of the cross-section, corresponding to the presence Cu–In alloy (Fig. 1g, h). However, a distinct concentrated distribution of Zn can be clearly observed beneath the region with enrichment of Cu and In (Fig. 1f). The variations in cross-sectional height can lead to different degrees of X-ray signal obstruction, resulting in a significant decrease in the intensity of EDS (energy dispersive X-ray spectroscopy) signals with increasing depth. In light of this, a gradual increase in the relative intensity of zinc

can still be observed from the line scanning analysis of EDS (Fig. 1e), while copper and indium exhibit a corresponding decrease with depth, which strongly suggests the presence of a zinc-rich transition phase between Cu–In layer and Zn substrate. The displacement reaction of Cu–In initiates from the surface and progresses along the grain boundary towards the bulk phase⁴⁷. As the reaction depth increases, the concentration and reactivity of the Cu–In solution decrease, leading to the emergence of a transition phase with an increasing zinc-content gradient. Besides, a small amount of radical zinc particles remains within the Cu–In alloy layer, which reinforces the integration with the substrate, thus ensuring the structural stability of the interface. Notably, the cross-cut test manifests the good adhesive strength between the Cu–In alloy layer and the substrate (Supplementary Fig. 4), which is crucial for its proper functionality.

X-ray diffraction (XRD) is performed to further investigate the composition of the interface. As illustrated in Fig. 1j, the XRD spectrum reveals that the Cu–In interface is mainly composed of CuIn (PDF#00-035-1150)^{48–51} and Cu₁₁In₉ (PDF#00-041-0883), with a small amount of indium and unconverted zinc. Besides, the interplanar distance of 2.59 Å assigned to the CuIn (200) crystal face can be observed in the high-resolution transmission electron microscopy (HRTEM) image⁵⁰, presenting great consistence with the XRD results. Attentionally, the CuIn is a metastable phase which does not exist in the Cu–In phase diagram, but it can indeed be acquired under some mild synthesis conditions (Supplementary Fig. 5)^{49,52}.

Furthermore, the synchrotron radiation-based X-ray Absorption Fine Structure (XAFS) was performed to explore the electronic structure and local coordination environment around the copper and indium atoms in the Cu–In alloy layer. The X-ray absorption near-edge spectrum (XANES) of In K-edge is presented in Fig. 1k. Besides, the integration method was employed to obtain the edge energy (E_{edge}) in XANES regardless of the shape of curves, thus analyzing the valence states semiquantitatively (Supplementary Fig. 6 and Supplementary Table 2)^{53,54}. According to the normalized results, the E_{edge} of indium in Cu–In (27938.47 eV) is almost equal to that in In foil (27938.33 eV), suggesting that the indium exists as In⁰ in the Cu–In alloy. Besides, as presented in the XANES of indium K-edge (Fig. 1l), the E_{edge} of copper in Cu–In (8985.87 eV) is almost equal to that in Cu foil (8985.90 eV), indicating that the Cu also exists as Cu⁰ in the Cu–In alloy.

Moreover, the Fourier-transformed EXAFS (extended X-ray absorption fine structure) was analyzed to explore the local coordination structure in Cu–In alloy. As shown in the R space positions (phase-uncorrected distances, Fig. 1m) of In K-edge, the In–In peak appears at around 2.98 Å in In foil. However, the intensity of this peak is significantly reduced in Cu–In, and a new peak assigned to the Cu–In peak appears at 2.47 Å, which coincides with that the Cu–In bond is shorter than the Cu–Cu bond. Besides, as illustrated in Fig. 1n, the Cu–Cu peak in Cu foil is 2.24 Å, while that is observed at 2.26 Å in the Cu–In. According to the fitting results of Cu K-edge EXAFS (Fig. 1o, p and Supplementary Table 3), there are two coordination bonds in Cu–In alloy (Cu–Cu, -2.54 Å, Cu–In, -2.79 Å), verifying the formation of Cu–In alloy. Moreover, as described in the wavelet transform (WT) results of Cu K-edge (Supplementary Fig. 7a, b), the relatively strong oscillation in the high-R part shifts to the higher wavenumber of k in the presence of indium, indicating the influence of indium on Cu. Besides, the strongest oscillation shifts to the lower wavenumber of k in the WT results of In K-edge with the existence of copper (Supplementary Fig. 7c, d), and no peaks appearing at the low wavenumber of k which belongs to the coordination with light elements, thus confirming the reciprocal coordination of Cu and In in the Cu–In alloy layer⁵⁵.

Investigation of zincophilicity and hydrogen evolution anticatalytic kinetics

To investigate the functionalities of copper and indium for Zn negative electrode, respectively, the Cu@Zn and In@Zn are also prepared using

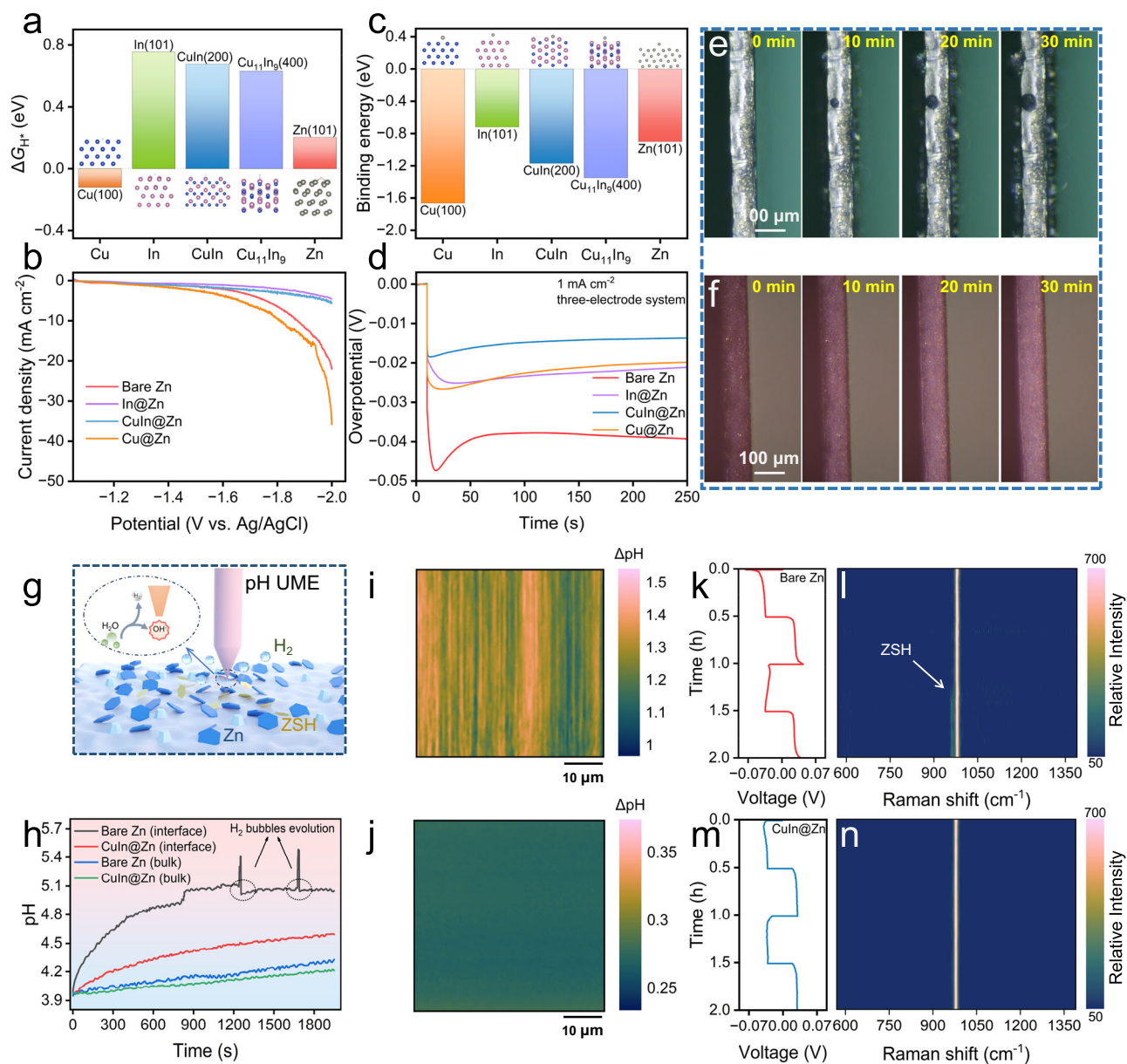


Fig. 2 | Quantitative descriptions for zincophilicity and side reactions. **a** ΔG_{H^+} and corresponding adsorption configurations of an H atom on different crystal faces. **b** LSV curves on different electrodes in 0.5 M Na_2SO_4 solution (3-electrode without IR-corrected, WE: Zn foils, CE: Pt foil electrode, RE: Ag/AgCl electrode, 25 °C). **c** Binding energy and corresponding adsorption configurations of a Zn atom on different crystal faces. **d** Chronopotentiometry curve of different electrodes in a three-electrode-system at the scanning rate of 1 mV s^{-1} (3-electrode without IR-corrected, WE: Zn foils, CE: bare Zn foils, RE: Ag/AgCl electrode, 25 °C). **e, f** In situ optical microscope pictures of Zn deposition on **e** bare Zn electrode and **f** CuIn@Zn

at a current density of 10 mA cm^{-2} (symmetric cells). **g** Schematic illustration of in situ interfacial pH detection by pH UME. **h** In situ interfacial pH evolution curves on different Zn electrodes at the plating current density of 10 mA cm^{-2} . **i, j** The mapping of interfacial pH changes on **i** bare Zn and **j** CuIn@Zn after soaking for 24 h. **k–n** In situ Raman spectra of **k, l** bare Zn and **m, n** CuIn@Zn negative electrode ($100 \mu\text{m}$ of thickness) cycling in the symmetric cell at the current density of 5 mA cm^{-2} for 2.5 mAh cm^{-2} and corresponding time-voltage curve. The thickness of Zn foils in above tests is $100 \mu\text{m}$.

the same method. At first, density functional theory (DFT) simulations and linear sweep voltammetry (LSV) were conducted to assess the influence of different substrates on HER. According to the HER-volcano⁵⁶, Cu, In, and Zn are on the left side, signifying that the rate-determining step of HER should be the electrochemical adsorption of H atoms or H_2O molecules on these surfaces¹⁸. As shown in Fig. 2a, In shows the highest Gibbs free energy of hydrogen adsorption (ΔG_{H^+}), indicating the weakest adsorption of H. Conversely, the ΔG_{H^+} on Cu is even positive, representing that Cu will catalyze the HER process. Fortunately, the introduction of In efficaciously mitigates the adsorption of H on the CuIn (200) and $\text{Cu}_{11}\text{In}_9$ (400) surfaces. The LSV curves

further confirm that the HER current density on Cu@Zn is even higher than bare Zn (Fig. 2b), while it is significantly reduced on In@Zn and CuIn@Zn, which is consistent with the simulation results. Besides, among Cu, In, and Zn, Cu^{2+}/Cu has the highest standard electrode potential (0.342 V vs. SHE , while In^{3+}/In is -0.338 V and Zn^{2+}/Zn is -0.762 V), thus the Cu is predictably able to suppress the chemical corrosion of Zn in aqueous electrolyte, which is verified in the polarization curve (Supplementary Fig. 8).

Subsequently, the zincophilicity of various substrates is quantified via DFT simulations and electrochemical tests. As shown in Fig. 2c, the Cu (100) shows the lowest binding energy while the In (101)

exhibits the highest binding energy, indicating the superior zincophilicity of Cu. Moreover, the binding energy of CuIn (200) and Cu₁₁In₉ (400) is lower than that of Zn and In, which reveals the Cu alloying evades the insufficient zincophilicity of In. Besides, the ΔG_{H^+} and zinc binding energy calculations for CuIn₂ and Cu₂In (two alloy phases with varying copper content) are conducted to validate the synergism of copper and indium in Cu–In alloys. As presented in Supplementary Fig. 9, both ΔG_{H^+} and zinc binding energy on Cu–In alloys fall within the range between those of pure copper and indium. Besides, there is an increasing trend observed in both ΔG_{H^+} and zinc binding energy on Cu–In alloys as the indium content increases, demonstrating the universality that the Cu–In alloy inherits the zincophilicity of copper and HER anticatalytic property from indium. As expected, the bare zinc electrode exhibits quite a high nucleation overpotential (47 mV) and deposition overpotential (39 mV) due to the poor zincophilicity (Fig. 2d). In contrast, both the Cu and In exhibit a lower overpotential, and CuIn@Zn demonstrates the lowest nucleation overpotential (18 mV) and deposition overpotential (13 mV), which is attributed to due to the zincophilicity of Cu and the reduced impedance of In resulting from decreased H adsorption³¹. Besides, according to the phase diagram of Zn–In (Supplementary Fig. 10), the metal indium is difficult to form an alloy with zinc⁵⁷, thus the indium is densely deposited on the surface of zinc to form a 2D substrate (Supplementary Fig. 11). The 3D structure of the Cu–In modified layer can not only significantly decrease the local current density, but also improve the wettability due to the capillary actions of porous nature (from 68.07° to 25.13°, Supplementary Fig. 12). Briefly, the good zincophilicity and improved wettability significantly reduce the conversion barrier from Zn²⁺ to Zn⁰ (Supplementary Fig. 13), meanwhile the 3D structure and rich zincophilic sites will lead to the rapid formation of fine but abundant Zn nuclei⁵⁸, reducing the resistance to their subsequent growth. As a result, from the in situ optical microscopy test (Fig. 2e, Supplementary Movie S1), many large Zn particles are observed generating on the surface of bare Zn randomly at the beginning of electrodepositing, which continue to grow at different speeds, leading to an uneven and granular Zn deposition layer. Whereas, Zn is deposited on the Cu–In alloy interface homogeneously and compactly during the entire process (Fig. 2f, Supplementary Movie S2). Accordingly, the Cu is helpful to improve zincophilicity, inhibit chemical corrosion, and result in uniform Zn nucleation, while the In is employed to avoid the HER in electrochemical process. As a result, the Cu–In combines the advantages of Cu and In, realizing the synergistic regulation of zinc deposition and HER kinetics.

The HER will result in the pH increase on the Zn/electrolyte interface, which serves as the immediate cause of the ZSH formation⁵⁹. To investigate the pH evolution at the interface, composite pH ultramicroelectrodes (pH-UME) equipped with scanning electrochemical microscopy (SECM) are utilized for in situ measurement of interfacial pH with high spatiotemporal resolution (Fig. 2g, Supplementary Fig. 14). In the self-made electrolytic cell, the pH detection site is located at 30 μm above the zinc electrode, which is in the diffusion layer of OH⁻⁶⁰. The spacing distance between pH-UME probe and the substrate electrode is controlled contactless by the current feedback of FcMeOH on the platinum ultra-microelectrodes⁶¹. As presented in Fig. 2h, the interfacial pH of the bare Zn increases rapidly to 5.1 within 850 s during the zinc deposition. Subsequently, a gradual rise in pH suggests the continuous formation of ZSH. Besides, the pH fluctuates dramatically at 1240 s and 1690 s, which can be attributed to disturbances caused by hydrogen bubble overflow. Conversely, no notable elevation in pH is observed on CuIn@Zn during zinc deposition, proving the substantial inhibition of both interfacial pH fluctuation and electrochemical HER process. In addition, there is a more severe HER if the bare Zn is porous (Supplementary Fig. 15). Considering the 3D structure and the larger specific surface area, the CuIn@Zn exhibits a more pH resistance than bare Zn. In addition,

SECM is employed for obtaining mappings depicting changes in interfacial pH on the Zn electrode. As presented in Fig. 2i, after soaking for 24 h, the interfacial pH of bare zinc unevenly and significantly increases for more than 1.0, indicating pronounced chemical corrosion due to the high activity of zinc metal and its uneven surface. By comparison, the interfacial pH of CuIn@Zn only increases by 0.3 (Fig. 2j), suggesting that the Cu–In layer effectively stabilizes the zinc electrode. Notably, the instability of interfacial pH will lead to the formation and accumulation of ZSH³³. In the Raman spectrum, there is a sharp peak located at 967 cm⁻¹ assigned to ZSH³⁷, which differs from the ZnSO₄ electrolyte (Supplementary Fig. 16). Based on this, in situ Raman spectra are employed for the in situ detection of ZSH. During the cycling of the Zn negative electrode, a peak at 967 cm⁻¹ appears on the bare zinc electrode in the second deposition process (Fig. 2k, l, Supplementary Fig. 17a). Besides, the peak persists in the subsequent stripping process, indicating the irreversible accumulation of ZSH. After being modified by the Cu–In layer, no new peaks appear throughout the entire cycle process (Fig. 2m, n, Supplementary Fig. 17b), indicating the Cu–In layer can significantly prevent the production of ZSH. Above all, CuIn@Zn enables the regulation of uniform Zn electrodeposition of zinc while inhibiting the accumulation of ZSH.

Preferred orientation of Zn (002) on Cu–In alloy interface

In fact, the zinc crystals always tend to be Zn (002) preferentially exposed hexagonal zinc flakes (HZF) during the electrochemical nucleation and growth (Supplementary Fig. 18)⁶². However, the HZFs will grow and stack to form EDZs (electrodeposited Zn) with diverse arrangements due to the influence of substrate zincophilicity, ion concentration distribution, and by-product accumulation⁵, resulting in the variety of texture⁶². Accordingly, the (101) and (100) crystal faces exhibit the HZF arranged at large angles or even vertically on the substrate, whereas the (002) face represents small angle or even parallel arrangements⁶². In addition, due to the strongest resistance to HER (Supplementary Fig. 19), achievement of preferred orientation Zn (002) has been the research focus for the Zn electrode optimization⁶³. Benefitting from the zincophilicity and the lattice structure diversity, conductive interfaces can affect the texture of EDZ significantly^{64,65}. Hence, the electrodeposition of Zn on various substrates is conducted to investigate the growth mechanism of EDZ. Besides, grazing incidence-XRD (GIXRD) was conducted to determine the texture distribution of EDZ, excluding the interference from the zinc substrate. As shown in Fig. 3a–d, the EDZ on CuIn@Zn presents a significant preference for Zn (002) over a wide range of deposited capacities, while preferential orientation of Zn (002) is observed on In@Zn and Cu@Zn only at the low deposition capacities, and bare Zn does not exhibit any preference for Zn (002) at any deposition capacities, indicating the achievement of ordered texture Zn deposition through synergistic regulation by Cu–In layer.

According to the growing process of EDZ, the critical factors for the preferred orientation of Zn (002) are horizontal growth during the initial stage and the subsequent layer stacking. Firstly, zincophilicity is the prerequisite for controlled zinc depositing on the substrate⁴². As illustrated in Supplementary Fig. 20a–c, a large number of fine nuclei are observed to grow uniformly on the surface of the Cu–In layer, indicating the rapid nuclei process. In addition, zincophobe Al foil and the CuIn@Al obtained through the similar co-replacement route were utilized in in situ XRD tests (Supplementary Fig. 21). As illustrated in Fig. 3e, with the increase of Zn deposition capacity on bare Al, the intensity of Zn (002) gradually increases but always maintains relatively weaker than Zn (100). The ratio of $I_{(002)}/I_{(100)}$ remains around 0.8 throughout the deposition process (Fig. 3g). For the CuIn@Al, the appearance of a weak peak (weakened due to the blocking of X-rays by Al foil) at around 34.5° confirms the existence of Cu–In alloy layer on Al foil (Fig. 3f). Notably, there is a rapid increase in Zn (002) intensity, with an $I_{(002)}/I_{(100)}$ ratio exceeding 3, significantly higher than that

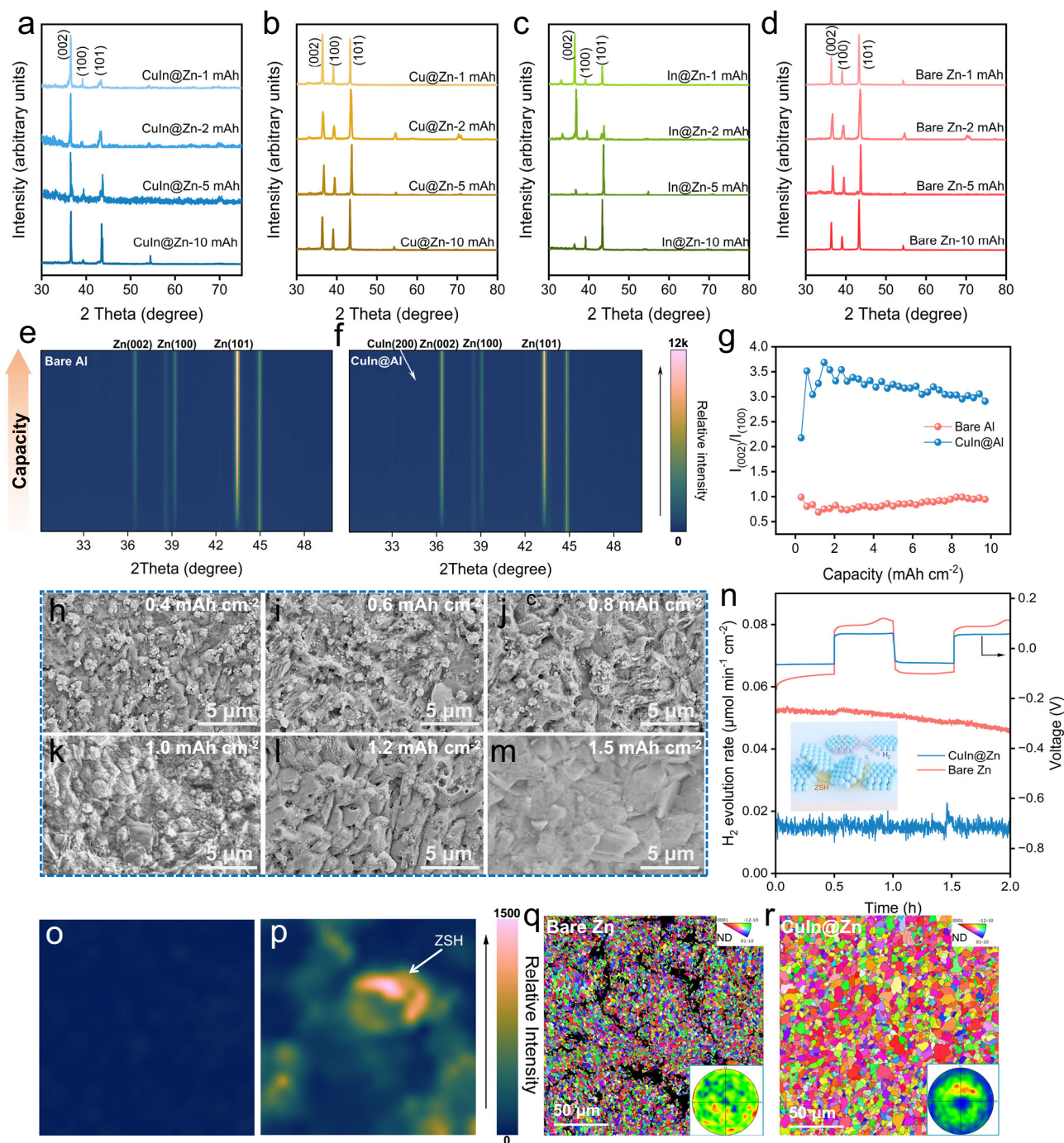


Fig. 3 | Preferred orientation of Zn (002) on Cu–In alloy interface. GIXRD patterns of Zn electrodepositions on **a** CuIn@Zn, **b** Cu@Zn, **c** In@Zn, and **d** bare Zn with different capacities at 1 mA cm⁻². The in situ XRD of electrodeposited Zn on **e** bare Al foil and **f** CuIn@Al at the current density of 5 mA cm⁻². **g** The intensity ratio of Zn (002) to Zn (100) at different deposition capacities during the in situ XRD tests. **h–m** The SEM images of CuIn@Zn after zinc deposition with different capacities at 1 mA cm⁻². **n** DEMS results in different Zn||Zn symmetric cells at

10 mA cm⁻² for 5 mA cm⁻² (inset is the schematic illustration of ZSH affecting the Zn electrodeposition). **o, p** Raman mapping of ZSH on **k** CuIn@Zn and **l** bare Zn and after 50 cycles at a current density of 1.0 mA cm⁻² for 1.0 mA cm⁻². **q, r** The inverse pole figure (IPFZ) orientation maps (inset is the corresponding Zn (002) pole figures) of **q** bare Zn and **r** CuIn@Zn after 5 mA cm⁻² deposition of zinc at 1 mA cm⁻². The thickness of Zn foils in above tests is 100 μm.

observed for bare Al substrates. This provides evidence that the Cu–In alloy layer effectively induces the preferred orientation of Zn (002), owing to its inherent zincophilicity independent of substrate influence. Moreover, on the zincophilic substrate, the orientation of HZF is notably influenced by substrate anisotropy⁶². Based on the extended formula for lattice mismatch calculating (reported by Zhou et al., Supplementary Fig. 22)⁶⁶, the Cu–In alloy layer can be assigned as the

semi-coherent interface, which helps reduce the interfacial energy during zinc deposition.

Due to the diffusion-induced distribution of Zn²⁺ concentration, the Zn deposition tends to occur at the tips (Supplementary Fig. 23e). However, it can be observed that zinc deposits at the bottom pits and evolves into a flat EDZ layer on CuIn@Zn (Supplementary Fig. 24). In fact, due to poor intrinsic conductivity of Cu–In and serious electron

scattering caused by abundant grain boundaries in nanoscale Cu–In primary particles, the conductivity of Cu–In powder is much lower than that of the substrate (Supplementary Fig. 23a–c). Considering the concentration gradient of zinc in the Cu–In alloy layer, the resistance gradient results in a significantly lower localized current density on the tips of bulges compared to that on the substrate, presenting the current density gradient from the bottom to the top (Supplementary Fig. 23d). As presented in Fig. 3h–m, the zinc deposition strictly starts at the bottom. Then the horizontally extending HZFs merge with each other, resulting in plate-like zinc deposition that covers the small Cu–In particles at the bottom. Subsequently, the HZFs continue to grow and stack until all Cu–In particles are covered. Throughout this process, HZFs maintain parallel arrangement with a low angle, corresponding to the preferential exposure of the Zn (002) crystal face. The gradient conductivity results in the bottom-up deposition of zinc in the 3D Cu–In layer, achieving dense and flat zinc deposition.

More importantly, insulated impurities such as ZSH accompanied with the HER will terminate the growth of HZF⁶⁷, causing stacking differences on the substrates, thereby resulting in the different texture of EDZ^{5,64,68}. As shown in the in situ differential electrochemical mass spectroscopy (DEMS, Fig. 3n) results, the rate of HER in real time is significantly reduced by Cu–In layer due to its HER-anticatalytic effect. As a result, there is barely ZSH accumulation on the surface of cycled CuIn@Zn (Fig. 3o), and the cycled CuIn@Zn is flat and dense (Supplementary Fig. 25a). The surface altitude of cycled CuIn@Zn is revealed to fluctuating within 300 nm (Supplementary Fig. 26a) by AFM (atomic force microscope). In contrast, due to the severe HER, the Raman mapping indicates the obvious accumulation of ZSH on the cycled bare Zn (Fig. 3p), which is responsible for the loose and mossy dendrites (Supplementary Fig. 25d) with a surface fluctuation of several microns (Supplementary Fig. 26b).

The limitation of a single regulation for HER kinetics or zincophilicity can be reflected from the EDZ on Cu@Zn or In@Zn surfaces. Well-defined and large HZF can be observed on the cycled Cu@Zn (Supplementary Fig. 25b), which is attributed to the strong zincophilicity of Cu. However, the high HER activity of Cu results in a significant accumulation of ZSH. As a result, the HZF on cycled Cu@Zn is unparallel to the substrate, and the EDZ on Cu@Zn exhibits a weak preference for Zn (002) only at a low deposition capacity (1 mAh cm⁻², Fig. 3b). By contrast, benefitting from its anti-HER ability, the EDZ on In@Zn has a significant preference for Zn (002) with low deposition capacities (1 mAh cm⁻² and 2 mAh cm⁻², Fig. 3c), and the EDZ on cycled In@Zn is pretty compact (Supplementary Fig. 25c). However, with the deposition capacity of EDZ on In@Zn increasing to 5 mAh cm⁻², the peak intensity of Zn (002) decreases notably, accompanied by the disappearance of In (101). Considering the 2D In layer is difficult to induce the bottom-up deposition and its zincophilicity is relatively weak, the In layer loses efficacy at a high-deposition capacity of EDZ, resulting in the uncontrollable HER and Zn deposition. The electron backscatter diffraction (EBSD) was performed to intuitively analyze the orientation distribution. As illustrated in Fig. 3q, numerous interspaces can be observed in the EDZ of bare Zn, while the grains are small and the texture is random due to the poor zincophilicity and serious HER. Besides, the Zn (002) shows an almost uniform distribution of intensity in the pole figure, suggesting a loose and non-texture orientation of EDZ. In contrast, the distribution of Zn (002) is significantly increased on the EDZ of CuIn@Zn. Moreover, the hotspot of Zn (002) is concentrated at the center of its pole figure (Fig. 3r), manifesting the preferential crystalline orientation of Zn (002) on the CuIn@Zn.

Therefore, the zincophilicity and low lattice mismatch of CuIn facilitate the growth of HZF along the substrate plane, while the 3D structure and bottom-up deposition properties originating from the gradient conductivity enable the ordered deposition. Moreover, the restrained accumulation of ZSH enhances the binding force between

HZFs and allows for their parallel arrangement, thus resulting in the flat and ZSH-free EDZ with Zn (002) preferential orientation. Therefore, it can be concluded that the Zn (002) preferential orientation on Cu–In alloy layer is the result of synergistic regulation involving the zincophilicity, HER-anticatalytic, and gradient conductivity structure, highlighting the meaning of synergistic regulation on Zn negative electrodes.

Self-construction and electrochemical performance

Firstly, the stability of the Cu–In alloy layer during the stripping process is verified through ex situ SEM and in situ optical microscopy tests. As shown in Supplementary Fig. 27, zinc is observed to be stripped beneath the Cu–In layer, which can remain basically intact even after a stripping capacity of 5 mAh cm⁻². Moreover, a half-replaced CuIn@Zn electrode was fabricated to compare the morphology evolution of the Cu–In layer and bare Zn during the stripping process simultaneously. As presented in Supplementary Fig. 28 and Supplementary Movie S3, as the duration of Zn stripping increases, the stripping traces begin to form on the bare Zn surface and progressively grows larger and uneven. By contrast, the Cu–In alloy layer remains stable throughout the discharging process without significant changes, indicating its remarkable stability. Besides, there was no obvious shedding of Cu–In particles on the cycled separator (Supplementary Fig. 28c), proving the cyclic stability of the Cu–In layer.

Notably, the Cu–In alloy layer will be self-constructed dynamically during the cycling process (Fig. 4a). As presented in the XRD pattern of cycled CuIn@Zn (Fig. 4b), a new diffraction peak at 33.0° is observed, which is assigned to the In (101)³². Besides, the relative intensity of the newly emerging peak is higher in the GIXRD pattern of cycled CuIn@Zn (Supplementary Fig. 29), indicating the phase separation of Cu–In alloy and the formation of indium metal on the surface. Compared to the pristine CuIn@Zn (Supplementary Fig. 1), many Cu–In particles disappear significantly after 10 cycles (Fig. 4c and Supplementary Fig. 30), with the surface being covered by blocky EDZ. After 20 cycles (Fig. 4d), the EDZ becomes flatter and the large Cu–In particles almost disappear, while the tiny Cu–In particles remain on the surface. After 50 cycles, no detectable copper is observed on the EDZ surface but numerous tiny indium particles are present (Fig. 4e), which coincides with the XRD results. From the perspective of thermodynamics, the standard electrode potentials of Cu, In, and Zn are 0.342 V, -0.338 V, and -0.762 V, respectively, thus the Cu is most stable during the cycling process. Moreover, it can be inferred from the phase diagram (Supplementary Fig. 31) that the Cu is easy to form alloys with Zn at room temperature. As described in Fig. 4a, since Cu can form an alloy with Zn but In cannot, the In will be slowly dissolved and replaced by Zn from the Cu–In alloy layer during the repeated zinc deposition/dissolution process. As presented in Supplementary Table 4, the indium demonstrates a more pronounced trend in dissolution and migration. In fact, the self-construction of Cu–In layer is a complicated process due to the presence of excessive zinc and pH fluctuations of electrolyte. The excessive electrolyte and lower pH levels promote the dissolution of indium due to reduced passivation effects⁴⁷. Besides, the dissolved In³⁺ will be reduced by zinc, thus the amount of dissolving indium is very small in the case of excessive zinc. In a macroscopic view, indium is removed from the alloy phase and migrates to the electrode surface, forming a gradient substrate with high indium content in the surface layer and high copper content in the inner layer. Since the electrode surface directly contacts with electrolyte leading to severe HER issues, this enrichment of indium significantly enhances its anti-HER capability. As presented in Fig. 4b, except CuIn@Zn, the new diffraction peaks of ZSH appear at 8.1° and 16.2° in the XRD patterns of other cycled electrodes. In addition, the enrichment of zincophilic Cu at the bottom is helpful to induce the bottom-up deposition of zinc, thus improving the utilization of the substrate. Consequently, the self-reconstruction of the

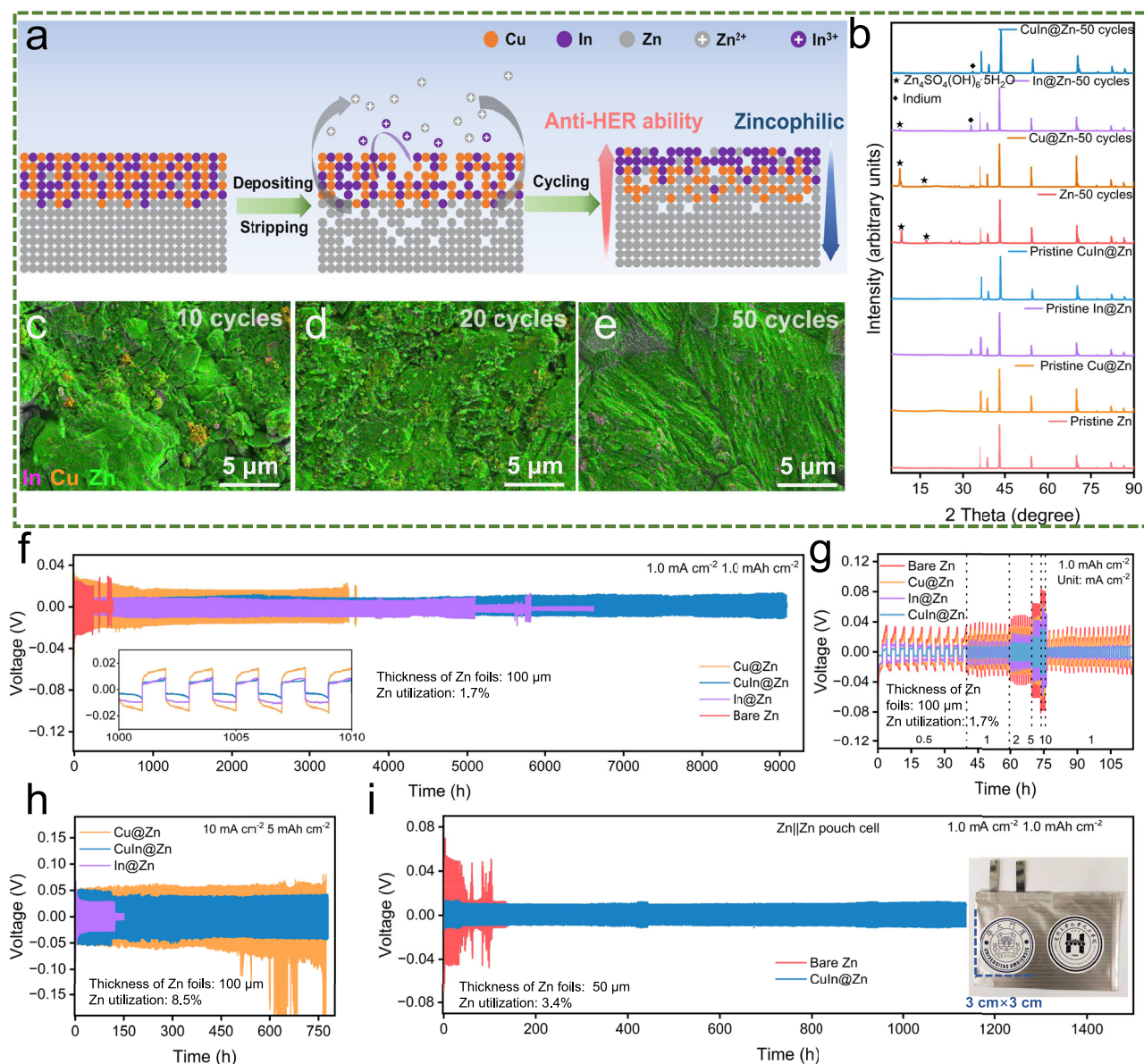


Fig. 4 | Self-construction and electrochemical performance of CuIn alloy interface. **a** Schematic illustration of self-construction of CuIn@Zn. **b** XRD patterns of the different pristine and cycled electrodes. **c–e** Morphology and element distribution evolution on CuIn@Zn after **c** 10 cycles, **d** 20 cycles, and **e** 50 cycles at a 1.0 mA cm⁻² for 1.0 mAh cm⁻² obtained by SEM. The voltage-time profiles of symmetric cells employing different electrodes at the conditions of **f** 1.0 mA cm⁻²,

1.0 mAh cm⁻² and **h** 10 mA cm⁻², 5 mAh cm⁻². **g** The rate performance of symmetric cells with different electrodes at current densities from 0.5 to 10 mA cm⁻². **i** The voltage-time profiles of symmetric pouch cells employing different electrodes at 1.0 mA cm⁻² for 1.0 mAh cm⁻² (inset is the digital photograph of CuIn@Zn||CuIn@Zn symmetric pouch cell).

CuIn@Zn substrate establishes a zincophilic and anti-HER gradient hierarchical structure, which further intensifies the effect of synergistic regulation.

The Zn||Zn symmetric cells are assembled to evaluate the cycling stability of various electrodes during long-term cycling. As presented in Fig. 4f, the CuIn@Zn||CuIn@Zn symmetric cell exhibits a long life-span of more than one year (9100 h) and a low voltage hysteresis (6 mV) at a current density of 1.0 mA cm⁻² with a plating/stripping capacity of 1.0 mAh cm⁻² (corresponding to the Zn utilization of 1.7% with the 100 μm Zn foils), which is superior than the majority of current reports about a conductive substrate designing (Supplementary Fig. 32 and Supplementary Table 5). By contrast, the short circuit occurs in In@Zn||In@Zn, Cu@Zn||Cu@Zn, and Zn||Zn symmetric cells at 5000 h, 3500 h, and 230 h, respectively. The rate performance of symmetric cells (Fig. 4g) shows that the CuIn@Zn displays the best

cycling stability and the smallest voltage hysteresis when the current density changes from 0.5, 1, 2, and 5 to 10 mA cm⁻². Even under a hard test condition of high current density and capacity (10 mA cm⁻², 5 mAh cm⁻², Fig. 4h), CuIn@Zn||CuIn@Zn symmetric cell achieves a long cyclic life of more than 750 h, while the In@Zn||In@Zn happens an internal short-circuit due to the failure of induced effect, and the Cu@Zn suffers from a severe polarization increase due to the serious HER. Besides, the CuIn@Zn||CuIn@Zn symmetric cells can also achieve a significant improvement of performance under other test conditions (Supplementary Fig. 33 and Supplementary Fig. 34), indicating the Cu–In modified layer can regulate the zinc deposition and dissolution over a broader range of current densities. Furthermore, electro-deposited zinc was utilized to restrict the zinc content and enhance the depth of charge and discharge (DOD). As shown in Supplementary Fig. 35, CuIn@Zn||CuIn@Zn symmetric cells with electro-deposited Zn

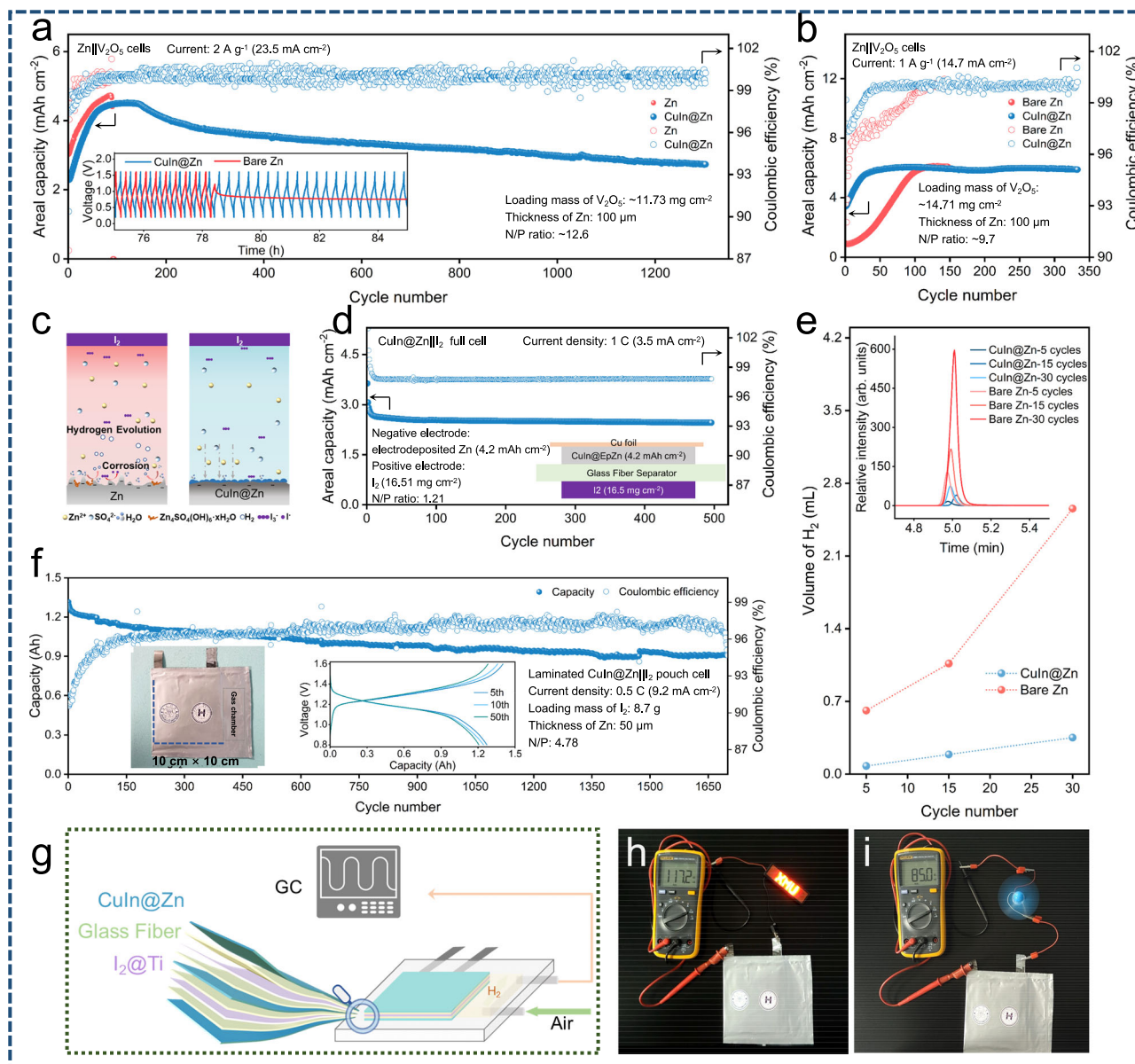


Fig. 5 | Application of CuIn@Zn negative electrode in high-capacity full cells. Cycling performance of Zn||V₂O₅ full cells employing different electrodes at **a** 2.0 A g⁻¹ and **b** 1.0 A g⁻¹ (inset is the corresponding time-voltage curve). **c** Schematic illustration of bare Zn deterioration and Cu-In layer improving the reversibility of Zn negative electrode in Zn||I₂ full cells. **d** Cyclic performance of CuIn@Zn||I₂ full cells with the electrodeposited Zn negative electrode at 1 C. **e** The H₂ evolution volume in different ampere-hour level Zn||I₂ pouch cells quantified by

GC and corresponding GC profiles. **f** Cyclic performance of ampere-hour level CuIn@Zn||I₂ pouch cell at 0.5 C (inset is the corresponding digital photograph and galvanostatic charge/discharge profiles). **g** Diagram of the stacked ampere-hour level CuIn@Zn||I₂ pouch and the quantity method of H₂. **h**, **i** The photos of ampere-hour level CuIn@Zn||I₂ pouch cell **h** lighting the LED panel and **i** driving the small electric fan.

can achieve a stable cyclic life of more than 700 h at the depth of charge and discharge (DOD) of 25%, and more than 500 h even if the DOD reaches 50%, indicating the effectiveness of Cu-In layer in enhancing the reversibility of Zn negative electrode.

Due to the larger area of electrodes and the smaller external pressure, the pouch cells require more stability of the electrode than the button cells. As expected, the CuIn@Zn||CuIn@Zn symmetric pouch cell (Fig. 4i) delivers a stable cyclic life of more than 1200 h with a small voltage hysteresis (10 mV) under the condition of 1.0 mA cm⁻² and 1.0 mAh cm⁻², while the internal short-circuit happens in the Zn||Zn pouch cells within only 40 h. Therefore, benefiting from the synergistic regulation and self-construction of the Cu-In alloy layer, the cycling reversibility and stability of the zinc negative electrode are significantly improved during long-term cycling.

Application in high-capacity full cells

Inspired by the synergistic regulation of the Cu-In alloy interface on suppressing HER and dendrite formation, V₂O₅ with high mass loading is employed as positive electrodes to evaluate the feasibility of CuIn@Zn. Notably, the higher mass loading of V₂O₅ means the more serious dissolution of vanadium species. The HER will lead to the increase of interfacial pH on the Zn electrode, resulting in the formation of insulating zinc vanadate, which will dramatically aggravate the dendrite growth on the Zn negative electrode^{69–71}. As presented in Fig. 5a, the capacity of Zn||V₂O₅ full cell drops to 0 after 228 cycles, and the time-voltage curve exhibits a sudden voltage drop during the charging process, indicating the occurrence of an internal short circuit in the cell. By contrast, CuIn@Zn||V₂O₅ delivers an average discharge capacity up to 3.36 mAh cm⁻² in more than 1300 cycles. At a low

current density of 1 A g^{-1} (Fig. 5b), the $\text{CuIn@Zn}||\text{V}_2\text{O}_5$ full cell can deliver a high discharge capacity of 6 mAh cm^{-2} in more than 330 cycles. At the current density of 3 A g^{-1} , the lifespan of $\text{CuIn@Zn}||\text{V}_2\text{O}_5$ full cell can be extended to more than 2000 cycles with an average areal discharge capacity of 2.86 mAh cm^{-2} (Supplementary Fig. 36). Even if assembled into pouch cells (Supplementary Fig. 37), the $\text{CuIn@Zn}||\text{V}_2\text{O}_5$ full cell can deliver a reversible capacity of 1.6 mAh cm^{-2} for 230 cycles at a low current density of 0.3 A g^{-1} , demonstrating the ability of Cu–In alloy interface to prevent the dendrite growth under extreme conditions.

In addition, the CuIn@Zn electrode is coupled with eco-friendly I_2 positive electrode to determine its reliability. Notably, the I_2 positive electrode, particularly with high loading mass, suffers from the serious shuttle effect of polyiodide intermediates (I_3^- , I_5^- , etc.), which will exacerbate the side reaction and cell degradation^{72–74}. Benefitting from the corrosion resistance of the Cu–In layer, the CuIn@Zn can not only synergistically regulate the HER and Zn deposition, but also prevent the Zn negative electrode from the severe I_3^- corrosion, thus enhancing the stability of full cells (Fig. 5c). As shown in Supplementary Fig. 38, even when employing a thin Zn foil ($20 \mu\text{m}$) with a high mass loading of I_2 (20 mg cm^{-2}) and limited N/P ratio of 2.74, the $\text{CuIn@Zn}||\text{I}_2$ full cell can deliver a high areal capacity of 2.81 mAh cm^{-2} in more than 2000 cycles at 2 C with good cyclic stability. With a lower Zn content in the negative electrode (4.2 mAh cm^{-2} , electrodeposited Zn, Fig. 5d), the full cell can deliver a high discharge capacity of 2.6 mAh cm^{-2} over 500 cycles at 1 C with a low N/P ratio of 1.21. Besides, the $\text{CuIn@Zn}||\text{I}_2$ pouch cell ($3 \text{ cm} \times 3 \text{ cm}$) can deliver an average reversible capacity of 17.3 mAh for more than 550 stable cycles at 2 C, while the $\text{Zn}||\text{I}_2$ pouch cell employing bare Zn negative electrode presents a dramatic capacity fluctuation within only 84 cycles and a significant increase of voltage hysteresis due to the serious HER and accumulation of by-products (Supplementary Fig. 39).

More importantly, the readily accessible CuIn@Zn facilitates the acquisition of ampere-hour-level zinc iodine batteries. As illustrated in Fig. 5e–g, the assembled ampere-hour level $\text{CuIn@Zn}||\text{I}_2$ pouch cell with a total loading mass of 8.7 g I_2 is laminated structurally, and the size of the electrode plate is $10 \text{ cm} \times 10 \text{ cm}$. Meanwhile, a gas chamber is set to mitigate the battery expansion and capture the generated H_2 for the gas chromatography (GC) test (Fig. 5g). As shown in Fig. 5e, with the protection of the Cu–In layer, the rate of hydrogen production decreased significantly. This enhancement enables the $\text{CuIn@Zn}||\text{I}_2$ pouch cell to deliver a high average capacity of 1.1 Ah stably for 1700 cycles (Fig. 5f), which is superior to most of the reported studies of rechargeable Zn metal pouch cells (Supplementary Fig. 40 and Supplementary Table 6). The acupuncture experiment confirms that the $\text{CuIn@Zn}||\text{I}_2$ pouch cell poses no security risks such as fire or explosion, aligning with consensus findings (Supplementary Fig. 41). Moreover, the assembled CuIn@Zn pouch cell is capable of lighting the LED panel (Fig. 5h, Supplementary Movie S4) and driving the small electric fan (Fig. 5i, Supplementary Movie S5) with a large and stable output current. Even with the limited Zn content in negative electrode (3.9 mAh cm^{-2} , electrodeposited Zn, Supplementary Fig. 42), the $\text{CuIn@Zn}||\text{I}_2$ pouch cell can exhibit a discharge capacity exceeding 16 mAh with an N/P ratio of 1.58, meanwhile successfully lighting an LED panel, proving the practical potential of Cu–In alloy layer modification strategy.

Discussion

Synergistic regulation of Zn zincophilicity and HER kinetics is executed to prevent the deterioration of the Zn negative electrode through an accessible Cu–In alloy interface, which combines the anti-HER capability of indium and the zincophilicity of copper. Besides, this work claims the interaction effect between HER, zinc deposition behavior, and ZSH accumulation via in situ scanning probe technology, Raman

spectroscopy, and theoretical simulations, reminding the importance of overall consideration of zincophilicity and HER. Moreover, the impressive performance of high-capacity $\text{CuIn@Zn}||\text{V}_2\text{O}_5$ full cells and ampere-hour level $\text{CuIn@Zn}||\text{I}_2$ pouch cell reveals the effect of synergistic regulation and the practicability of the Cu–In alloy modified layer. In the end, we hope this work can provide an opportunity for highly reversible practical Zn negative electrode, promoting the commercialization process of AZMBs.

Methods

Preparation of electrodes

The CuIn@Zn electrode was prepared by the chemical substitution method. In detail, $1.6 \text{ g InCl}_3 \cdot 4\text{H}_2\text{O}$ (Macklin, >99.9%) and $0.35 \text{ g CuCl}_2 \cdot 2\text{H}_2\text{O}$ (Aladdin, >99.9%) were dispersed in a mixed solvent containing 350 mL ethanol (Aladdin, >99.5%) and $30 \text{ mL ultra-pure water}$ (>18 M Ω) at room temperature (-25°C). Then, the polished Zn foils ($10 \text{ cm} \times 10 \text{ cm}$) were immersed in the obtained solution for 3 min. After that, the obtained CuIn@Zn plate was washed with ultra-pure water and ethanol, respectively. Similarly, the Cu@Zn and In@Zn were obtained in the same process, in which the distinction is that the mixed solution only contains the $\text{InCl}_3 \cdot 4\text{H}_2\text{O}$ (for In@Zn) or $\text{CuCl}_2 \cdot 2\text{H}_2\text{O}$ (for Cu@Zn). The obtained electrodes foils were all cut into discs ($\Phi 12 \text{ mm}$), strips ($1 \text{ cm} \times 2 \text{ cm}$) and square plates ($3 \text{ cm} \times 3 \text{ cm}$ or $10 \text{ cm} \times 10 \text{ cm}$) for tests of button cells, three-electrode system, and pouch cells, respectively. The Cu–In powder was separated from the CuIn@Zn through a mechanical stripping method. Typically, the CuIn@Zn foil was immersed in the ethanol, and the Cu–In layer was carefully removed from the surface using a lab scraper. Subsequently, these collected Cu–In particles, dispersed in ethanol, were separated through vacuum filtration and then washed three times with water and ethanol in turn. The sediment was freeze-dried to obtain the final Cu–In powder. To fabricate V_2O_5 positive electrodes, commercial V_2O_5 (Macklin, >99%), acetylene black (9DINGCHEM), and polyvinylidene fluoride (PVDF, SOLVAY SOLEF PVDF 5130) were mixed in N-methyl-2-pyrrolidone (NMP, SINOPHARM, >99%) solvent in a mass ratio of 7:2:1 to obtain a slurry with the magnetic stirring. The slurry was pasted onto 12 mm diameter hydrophilic conductive carbon cloth (Cetech) or stainless-steel mesh ($3 \text{ cm} \times 3 \text{ cm}$, for pouch cells) and dried at 80°C for 24 h in the vacuum oven, and the loading mass of V_2O_5 in positive electrodes was $11\text{--}15 \text{ mg cm}^{-2}$ (on carbon cloth) and $4\text{--}6 \text{ mg cm}^{-2}$ (on stainless-steel mesh). The I_2 positive electrode was obtained through a sublimation diffusion method on activated carbon cloth (ACC, $280 \mu\text{m}$ of thickness, 9.5 mg cm^{-2} of density) which was treated with 9 wt% hydrochloric acid. In detail, the ACC was pre-cut to discs ($\Phi 12 \text{ mm}$ for coin cells) and square plates ($3 \text{ cm} \times 3 \text{ cm}$ or $10 \text{ cm} \times 10 \text{ cm}$ for pouch cells). Then a certain amount of I_2 (Aladdin, >99.8%) and ACC were mixed in a sealed glassy reactor and then heated at 80°C for 30 min, and the loading mass of I_2 in positive electrodes was $20\text{--}25 \text{ mg cm}^{-2}$. Notably, to enhance the conductivity and support of the positive electrode matrix in $\text{Zn}||\text{I}_2$ pouch cells, the ACC@I_2 was bonded to the Ti foils ($3 \text{ cm} \times 3 \text{ cm}$ or $10 \text{ cm} \times 10 \text{ cm}$, $30 \mu\text{m}$ of thickness) with homemade aqueous conductive adhesive (containing acetylene black, carboxymethyl cellulose, and polymerized styrene butadiene rubber with a mass ratio of 9:0.5:0.5).

Electrochemical measurements

$\text{Zn}||\text{Zn}$ symmetric cells, $\text{Zn}||\text{V}_2\text{O}_5$ full cells, and $\text{Zn}||\text{I}_2$ full cells were assembled into pouch cells or CR-2032 type coin cells and tested with the Neware BTS test system at 25°C . The full cells were charged to 1.6 V (for both V_2O_5 and I_2 positive electrodes), and discharged to 0.8 V (for I_2 positive electrode) or 0.2 V (for V_2O_5 positive electrode) in constant current mode. The glass fiber filters (GF-D, Whatman, $675 \mu\text{m}$ of thickness) were employed as the separator. The volume of electrolyte was $120 \mu\text{L}$ (for coin cells), $800 \mu\text{L}$ (for $3 \text{ cm} \times 3 \text{ cm}$ pouch cells), and

25 mL (for Ah-level Zn|| I_2 pouch cell). The pure 2.0 M ZnSO_4 (Aladdin, >99.5%) was employed as electrolyte for all the cells except the Zn|| V_2O_5 full cells. For the Zn|| V_2O_5 full cells, 3.0 M zinc trifluoromethylsulfonate ($\text{Zn}(\text{OTf})_2$, LEYAN, >98%) was employed as the electrolyte of Zn|| V_2O_5 to avoid the severe dissolution of V_2O_5 . Besides, cellulose membrane was employed as the additional separator to reduce the influence of V_2O_5 dissolution, and the cells were activated for 5 cycles at 0.1 A g^{-1} to improve the capacity (Supplementary Fig. 43). The Ah-level Zn|| I_2 pouch cells were laminated configuration which consisted of two layers of positive electrodes, three layers of negative electrodes, and four layers of separators. Both the positive and negative electrodes were double-side coated. Specifically, the carbon cloths with loading of I_2 ($10 \text{ cm} \times 10 \text{ cm}$) were adhered on two sides of titanium foils ($10 \text{ cm} \times 10 \text{ cm}$, thickness of $30 \mu\text{m}$), while both sides of the zinc foil negative electrodes ($10 \text{ cm} \times 10 \text{ cm}$, thickness of $50 \mu\text{m}$) were modified with the Cu–In layers. The total mass of all components for assembled Ah-level Zn|| I_2 pouch cells is 65–75 g. The LSV curves for HER, polarization curves, and chronopotentiometry curves were obtained in the three-electrode cells (50 mL of size, with the addition of 10 mL electrolyte) at 25°C . Electrochemical workstation (CHI 660E, chinstruments) was employed to collect the data without current-resistance corrected. The Ag/AgCl (in 3 M KCl) electrode that calibrated in the reversible hydrogen electrode system was utilized as the reference electrode. The $1 \text{ cm} \times 2 \text{ cm}$ pristine Zn foils or modified Zn foils (CuIn@Zn, Cu@Zn, and In@Zn) were employed as working electrodes. The back of Zn foils was insulated by polyimide tapes, and the area of working electrodes exposed in electrolyte was controlled as 1 cm^2 . The current in 3-electrode systems were normalized with area. The tests for HER were performed with the LSV program from -1.0 V to -2.0 V at a scanning rate of 1 mV s^{-1} , in which $1 \text{ cm} \times 1 \text{ cm}$ platinum plate electrode was employed as counter electrode, and $0.5 \text{ M Na}_2\text{SO}_4$ solution was selected as supporting electrolyte to avoid the influence of Zn electrodeposition. For polarization curves and chronopotentiometry curves, pure Zn foils were employed as the counter electrode in the 2 M ZnSO_4 electrolyte. Polarization curves were obtained by the TAFEL program at a scanning rate of 1 mV s^{-1} from -0.84 V to -1.14 V . The chronopotentiometry curves were obtained by the MULTI-CURRENT STEPS program with a current density of -1 mA cm^{-2} . Electrochemical impedance spectroscopy tests were performed by Solartron1287A + 1260 A (AMETEK) in Zn||Zn symmetric cells. The in situ localized pH tests were performed on the scanning an electrochemical microscope (SECM, CHI920d, chinstruments) equipped with the homemade composite pH ultramicroelectrode (UME)³³. The pH UME consisted of Pt ($\Phi 20 \mu\text{m}$), W/ WO_3 ($\Phi 50 \mu\text{m}$), and Ag/AgCl electrode, working as range-indicating electrode, pH-responsive electrode, and reference electrode, respectively. The potential of the W/ WO_3 electrode is Nernst corresponding to the concentration of protons, thus the open circuit potential of pH UME has a linear relationship with the pH of the solution, and the pH was calculated from the following equation (the unit of E is V): $\text{pH} = -24.07E + 1.120$. Pristine Zn foil or CuIn@Zn of $0.5 \text{ cm} \times 0.5 \text{ cm}$ was located in the bottom of self-made electrochemical cell as substrate electrode. By the current feedback of Pt UME in 1.0 mM ferrocene methanol (FcMeOH, with the addition of 0.1 M KCl), the vertical distance between the W/ WO_3 electrode and substrate electrode was controlled at $30 \mu\text{m}$. In the in situ interfacial pH tests, electrodes for Zn electrodeposition were arranged properly and powered by a direct-current source, thus avoiding the interference of the pH UME potential by the solution electric field. In the mapping of interfacial pH change, the electrolyte is replaced with 1 M NaCl solution to accelerate the corrosion process.

Materials characterizations

The ICP-OES was performed on SPECTRO SPECTROBLUE FMX36. The GIXRD patterns were obtained by Rigaku Ultima IV X-ray powder

diffractometer (Cu-K α , 40 KV, $3^\circ/\text{min}$). The XRD and in situ XRD tests were performed on the X-ray diffractometer (Malvern PANalytical Empyrean diffractometer with Cu K α radiation) within the homemade electrochemical cell. The EBSD was performed on Nordlys max3, and the samples were polished by Ar ions. The XAFS data were collected through the Shanghai Synchrotron Radiation Facility (SSRF, BL11B) with Si (111) crystal monochromators for Cu K-edge and Si (311) crystal monochromators for In K-edge, respectively. The In K-edge XAFS spectra were recorded in fluorescence mode, while the Cu K-edge spectra were obtained in transmission mode. The FIB processing was conducted on the Orion Nanofab. The XPS profile was obtained by Thermo Scientific ESCALAB Xi+ (Al-K α , 1486.68 eV). The field emission scanning electron microscopy images (SEM) were acquired by Zeiss GeminiSEM 500 (EHT = 5 kV). Atomic force microscope (AFM) images were obtained by Oxford Instruments Asylum Research Cypher ES. The in situ optical images were acquired on a CX40M metallographic microscope (NINGBO SUNNY INSTRUMENTS) with a homemade electrochemical cell at 10 mA cm^{-2} . The microstructure of Cu–In alloy particles and the corresponding element mapping were observed through transmission electron microscopy (TEM, FEI Tecnai F30). The specific resistance of Cu–In powder was measured by resistivity testers (ST2742B for low resistance and ST2463 for high resistance, four probe method). The electrodes for materials characterizations are all cycled in CR2032 type coin symmetric cells for different cycles (generally 50 cycles), and washed with deionized water to get rid of the ZnSO_4 on the surface. Raman spectroscopy (Horiba LabRAM HR Evolution) was used to characterize the ZSH on the surface of the electrode, with a 532 nm wavelength of laser and 28 mW power. The GC results were obtained by (Agilent Technologies 7890 A). For GC tests, 20 mL of normal air (79% nitrogen) was injected into the gas chamber to dilute the hydrogen. Then all of the gas was pumped to GC for H_2 concentration, and the H_2 volume was inferred according to the intensity of N_2 . The nail penetration test was conducted by a battery nail penetration tester (DGBELL) with a 3 mm diameter stainless steel nail. The DEMS test was conducted on HPR-40, R&D with a homemade stainless steel electrochemical cell that ensures great airtightness and achieve well conductive connection of electrode slice at the same time. The electrochemical cells were cycled with a configuration of symmetric cells at 1 mA cm^{-2} for 1 mAh cm^{-2} . Meanwhile, the generated gas (H_2) during cycling was blown out continuously of the cell by pure argon (the flow rate is 5 mL min^{-1}). After removing the water by passing through the -15°C cold trap, the mixture gas is analyzed by a mass spectrometer. And the signal intensity of hydrogen was calibrated by standard gas containing 100 ppm of H_2 .

Simulations and DFT calculations

All the phase diagrams in this work were obtained through the FactSageTM thermochemical software⁷⁵. The DFT calculations were carried out using the Vienna Ab initio Simulation Package (VASP)⁷⁶. The core electrons were modeled with the projector-augmented-wave (PAW) method⁷⁷. The exchange and correlation function of Perdew–Burke–Ernzerhof (PBE) was adopted within the framework of generalized gradient approximation (GGA)⁷⁸. The plane-wave basis cut-off energy was set to 500 eV. The structures were relaxed until the forces and total energy on all atoms converged to less than 0.02 eV \AA and $1 \times 10^{-5} \text{ eV}$, respectively. Visualization of the structures is made by using VESTA software. To explore the interactions between a Zn or H atom and substrates cleaved from the corresponding crystal structure, a vacuum layer of 15 \AA was adopted.

Based on the experimental data (XRD results), the main exposed surfaces of different substrates (Zn (101), Cu (100), In (101), CuIn (200), $\text{Cu}_{11}\text{In}_9$ (400)) are chosen to build the model. Zn atom adsorption energy calculations: The binding energies of Zn atom on Zn (101), Cu (100), In (101), CuIn (200), $\text{Cu}_{11}\text{In}_9$ (400), CuIn_2 (100), and Cu_2In (100)

surfaces were calculated according to the Eq. 1:

$$E_a = E_{\text{Zn-substrate}} - E_{\text{substrate}} - E_{\text{Zn}} \quad (1)$$

where $E_{\text{Zn-substrate}}$ is the energy of a Zn atom adsorbed on the Zn surface, $E_{\text{substrate}}$ is the energy of the Zn slab and E_{Zn} is the energy of a single Zn atom.

Gibbs free energy change ΔG_{H^*} calculation: The Gibbs free energy changes ΔG_{H^*} of hydrogen evolution reactions on Zn (101), Cu (100), In (101), CuIn (200), $\text{Cu}_{11}\text{In}_9$ (400), CuIn_2 (100), and Cu_2In (100) surfaces were calculated according to the Eq. 2:

$$\Delta G = \Delta E_{\text{H}} + \Delta E_{\text{ZPE}} - T\Delta S_{\text{H}} \quad (2)$$

Where ΔE_{ZPE} is the difference in zero point energy and ΔS_{H} is the entropy between hydrogen adsorption and hydrogen in the gas phase. Here the contributions from the electrode to both ΔE_{ZPE} and ΔS_{H} are small and could be neglected. As a result, the ΔE_{ZPE} is obtained by Eq. 3 and Eq. 4, in which $S_{\text{H}_2}^0$ is the entropy of H_2 gas at the standard condition.

$$\Delta E_{\text{ZPE}} = E_{\text{ZPE}}^{\text{H}} - 1/2E_{\text{H}_2} \quad (3)$$

$$\Delta S_{\text{H}} \cong -1/2S_{\text{H}_2}^0 \quad (4)$$

The binding energy of H atom adsorption on the surface of the supercell was obtained according to the following Eq. 5, where $E_{\text{sub}}^{\text{H}}$ is the energy of an atom adsorbed on the electrode substrate, E_{sub} is the energy of the substrate, and E_{H_2} is the energy of gas H_2 .

$$\Delta E_{\text{H}} = E_{\text{sub}}^{\text{H}} - E_{\text{sub}} - 1/2E_{\text{H}_2} \quad (5)$$

Data availability

The data supporting this study have been included in the main text and Supplementary Information. The other relevant data supporting this work are available from the corresponding authors on request. Source data are provided with this paper.

References

- Cai, W. et al. The boundary of lithium plating in graphite electrode for safe lithium-ion batteries. *Angew. Chem. Int. Ed.* **60**, 13007–13012 (2021).
- Cong, J. et al. Ultra-stable and highly reversible aqueous zinc metal anodes with high preferred orientation deposition achieved by a polyanionic hydrogel electrolyte. *Energy Storage Mater.* **35**, 586–594 (2021).
- Wang, X. et al. Ether–water hybrid electrolyte contributing to excellent mg ion storage in layered sodium vanadate. *ACS Nano* **16**, 6093–6102 (2022).
- Liu, Y. et al. Rechargeable aqueous Zn-based energy storage devices. *Joule* **5**, 2845–2903 (2021).
- Zou, Y. et al. Emerging strategies for steering orientational deposition toward high-performance Zn metal anodes. *Energy Environ. Sci.* **15**, 5017–5038 (2022).
- Hao, J. et al. Deeply understanding the Zn anode behaviour and corresponding improvement strategies in different aqueous Zn-based batteries. *Energy Environ. Sci.* **13**, 3917–3949 (2020).
- Liu, Z. et al. Voltage issue of aqueous rechargeable metal-ion batteries. *Chem. Soc. Rev.* **49**, 180–232 (2020).
- Liang, Y., Dong, H., Aurbach, D. & Yao, Y. Current status and future directions of multivalent metal-ion batteries. *Nat. Energy* **5**, 646–656 (2020).
- Zhang, Q., Luan, J., Tang, Y., Ji, X. & Wang, H. Interfacial design of dendrite-free zinc anodes for aqueous zinc-ion batteries. *Angew. Chem. Int. Ed.* **59**, 13180–13191 (2020).
- Lin, L. et al. A semi-conductive organic cathode material enabled by extended conjugation for rechargeable aqueous zinc batteries. *Energy Environ. Sci.* **16**, 89–96 (2023).
- Ma, L. et al. Realizing high zinc reversibility in rechargeable batteries. *Nat. Energy* **5**, 743–749 (2020).
- Yang, Q. et al. Dendrites in Zn-based batteries. *Adv. Mater.* **32**, 2001854 (2020).
- Liu, H. et al. Rechargeable aqueous zinc-ion batteries: mechanism, design strategies and future perspectives. *Mater. Today* **42**, 73–98 (2021).
- Verma, V., Kumar, S., Manalastas, W. & Srinivasan, M. Undesired reactions in aqueous rechargeable zinc ion batteries. *ACS Energy Lett.* **6**, 1773–1785 (2021).
- Zhang, J. et al. Nonepitaxial electrodeposition of (002)-textured Zn anode on textureless substrates for dendrite-free and hydrogen evolution-suppressed Zn batteries. *Adv. Mater.* **35**, e2300073 (2023).
- Zhang, T. et al. Fundamentals and perspectives in developing zinc-ion battery electrolytes: a comprehensive review. *Energy Environ. Sci.* **13**, 4625–4665 (2020).
- Zhao, Z. et al. Revealing the missing puzzle piece of concentration in regulating Zn electrodeposition. *Proc. Natl Acad. Sci. USA* **120**, e2307847120 (2023).
- Chen, J. et al. Challenges and perspectives of hydrogen evolution-free aqueous Zn-ion batteries. *Energy Storage Mater.* **59**, 102767 (2023).
- Huang, C. et al. Selection criteria for electrical double layer structure regulators enabling stable Zn metal anodes. *Energy Environ. Sci.* **16**, 1721–1731 (2023).
- Wang, T. et al. Spirally grown zinc-cobalt alloy layer enables highly reversible zinc metal anodes. *Adv. Funct. Mater.* **33**, 2306101 (2023).
- Wang, L. et al. Sn alloying to inhibit hydrogen evolution of Zn metal anode in rechargeable aqueous batteries. *Adv. Funct. Mater.* **32**, 2108533 (2021).
- Fayette, M., Chang, H. J., Rodri Guez-Perez, I. A., Li, X. & Reed, D. Electrodeposited zinc-based films as anodes for aqueous zinc batteries. *ACS Appl. Mater. Interfaces* **12**, 42763–42772 (2020).
- Zhang, Y., Howe, J. D., Ben-Yoseph, S., Wu, Y. & Liu, N. Unveiling the origin of alloy-seeded and nondendritic growth of Zn for rechargeable aqueous Zn batteries. *ACS Energy Lett.* **6**, 404–412 (2021).
- Liu, Z. et al. Dendrite-free nanocrystalline zinc electrodeposition from an ionic liquid containing nickel triflate for rechargeable Zn-based batteries. *Angew. Chem. Int. Ed.* **55**, 2889–2893 (2016).
- Tribbia, M., Glenneberg, J., Zampardi, G. & La Mantia, F. Highly efficient, dendrite-free zinc electrodeposition in mild aqueous zinc-ion batteries through indium-based substrates. *Batteries Supercaps* **5**, e202100381 (2022).
- Zhao, R. et al. Prioritizing hetero-metallic interfaces via thermodynamics inertia and kinetics zincophilia metrics for tough Zn-based aqueous batteries. *Adv. Mater.* **35**, 2209288 (2023).
- Zheng, X. et al. Constructing robust heterostructured interface for anode-free zinc batteries with ultrahigh capacities. *Nat. Commun.* **14**, 76 (2023).
- Cai, Z. et al. Chemically resistant Cu–Zn/Zn composite anode for long cycling aqueous batteries. *Energy Storage Mater.* **27**, 205–211 (2020).
- Zeng, Y. et al. Nitrogen-doped carbon fibers embedded with zincophilic Cu nanoboxes for stable Zn-metal anodes. *Adv. Mater.* **34**, 2200342 (2022).

30. Kao, C. C. et al. Suppressing hydrogen evolution via anticatalytic interfaces toward highly efficient aqueous Zn-Ion batteries. *ACS Nano* **17**, 3948–3957 (2023).
31. Xiao, P. et al. An anticorrosive zinc metal anode with ultra-long cycle life over one year. *Energy Environ. Sci.* **15**, 1638–1646 (2022).
32. Ouyang, K. et al. A new insight into ultrastable Zn metal batteries enabled by in situ built multifunctional metallic interphase. *Adv. Funct. Mater.* **32**, 2109749 (2021).
33. Zhang, M. et al. Dynamically interfacial pH-buffering effect enabled by N-methylimidazole molecules as spontaneous proton pumps toward highly reversible zinc metal anodes. *Adv. Mater.* **35**, 2208630 (2023).
34. Yuan, L. et al. Regulation methods for the Zn/electrolyte interphase and the effectiveness evaluation in aqueous Zn-ion batteries. *Energy Environ. Sci.* **14**, 5669–5689 (2021).
35. Yang, Y. et al. Synergistic manipulation of Zn²⁺ ion flux and desolvation effect enabled by anodic growth of a 3D ZnF₂ matrix for long-lifespan and dendrite-free Zn metal anodes. *Adv. Mater.* **33**, 2007388 (2021).
36. Wang, D. et al. Rational screening of artificial solid electrolyte interphases on Zn for ultrahigh-rate and long-life aqueous batteries. *Adv. Mater.* **35**, 2207908 (2023).
37. Zhao, Z. et al. Horizontally arranged zinc platelet electrodeposits modulated by fluorinated covalent organic framework film for high-rate and durable aqueous zinc ion batteries. *Nat. Commun.* **12**, 6606 (2021).
38. Ke, J. et al. Tailoring anion association strength through polycation-anion coordination mechanism in imidazole polymeric ionic liquid-based artificial interphase toward durable Zn metal anodes. *Adv. Funct. Mater.* **33**, 2301129 (2023).
39. Zheng, S. et al. In situ polymerization of ionic liquid with tunable phase separation for highly reversible and ultralong cycle life Zn-Ion battery. *Nano Lett.* **22**, 9062–9070 (2022).
40. Gao, Y. et al. Stable Zn anodes with triple gradients. *Adv. Mater.* **35**, 2207573 (2022).
41. Liang, G. et al. Gradient fluorinated alloy to enable highly reversible Zn-metal anode chemistry. *Energy Environ. Sci.* **15**, 1086–1096 (2022).
42. Li, H. et al. Trade-off between zincophilicity and zincophobicity: toward stable Zn-based aqueous batteries. *JACS Au* **3**, 2107–2116 (2023).
43. Yang, J.-L. et al. Dielectric-metallic double-gradient composition design for stable Zn metal anodes. *ACS Energy Lett.* **8**, 2042–2050 (2023).
44. Wang, Y. et al. Sulfolane-containing aqueous electrolyte solutions for producing efficient ampere-hour-level zinc metal battery pouch cells. *Nat. Commun.* **14**, 1828 (2023).
45. Wang, Y. et al. Manipulating electric double layer adsorption for stable solid-electrolyte interphase in 2.3 Ah Zn-Pouch cells. *Angew. Chem. Int. Ed.* **62**, e202302583 (2023).
46. Shinde, S. S. et al. Scaling-up insights for zinc-air battery technologies realizing reversible zinc anodes. *Adv. Mater.* **35**, 2303509 (2023).
47. Cai, Z. et al. A replacement reaction enabled interdigitated metal/solid electrolyte architecture for battery cycling at 20 mA cm⁻² and 20 mAh cm⁻². *J. Am. Chem. Soc.* **143**, 3143–3152 (2021).
48. Simić, V. & Marinković, Ž. Room temperature interactions in copper-metal thin film couples. *J. Less-Common Met* **72**, 133–140 (1980).
49. Chang, J. et al. Bimetallic nanoparticles of copper and indium by borohydride reduction. *Thin Solid Films* **519**, 2176–2180 (2011).
50. Li, L. et al. Crystal facet engineering coexposed CuIn (200) and In (101) in CuIn alloy nanocatalysts enabling selective and stable CO₂ electroreduction. *J. Energy Chem.* **86**, 569–578 (2023).
51. Ishizaki, T., Saito, N. & Fuwa, A. The effect of citric acid and EDTA addition on Cu-In alloy electrochemical deposition. *Mater. Trans., JIM* **40**, 867–870 (1999).
52. Barrado, E., García, S., Rodríguez, J. A. & Castrillejo, Y. Electrodeposition of indium on W and Cu electrodes in the deep eutectic solvent choline chloride-ethylene glycol (1:2). *J. Electroanal. Chem.* **823**, 106–120 (2018).
53. Tang, Y. et al. Sustainable layered cathode with suppressed phase transition for long-life sodium-ion batteries. *Nat. Sustain* **7**, 348–359 (2024).
54. Cao, X. et al. Reversible anionic redox chemistry in layered Li₄/₇[Y_{1/7}Mn_{6/7}]O₂ enabled by stable Li-O-vacancy configuration. *Joule* **6**, 1290–1303 (2022).
55. Song, J. et al. Phase-separated Mo-Ni alloy for hydrogen oxidation and evolution reactions with high activity and enhanced stability. *Adv. Energy Mater.* **11**, 2003511 (2021).
56. Zeradjanin, A. R., Grote, J.-P., Polymeros, G. & Mayrhofer, K. J. J. A critical review on hydrogen evolution electrocatalysis: re-exploring the volcano-relationship. *Electroanalysis* **28**, 2256–2269 (2016).
57. Fayette, M., Chang, H. J., Li, X. & Reed, D. High-performance InZn alloy anodes toward practical aqueous zinc batteries. *ACS Energy Lett.* **7**, 1888–1895 (2022).
58. Yang, J.-L., Yang, P., Yan, W., Zhao, J.-W. & Fan, H. J. 3D zincophilic micro-scaffold enables stable Zn deposition. *Energy Storage Mater.* **51**, 259–265 (2022).
59. Yang, Q. et al. Stabilizing interface pH by N-modified graphdiyne for dendrite-free and high-rate aqueous Zn-Ion batteries. *Angew. Chem. Int. Ed.* **61**, 202112304 (2021).
60. Kwak, J. & Bard, A. J. Scanning electrochemical microscopy. Theory of the feedback mode. *Anal. Chem.* **61**, 1221–1227 (1989).
61. Shi, X., Qing, W., Marhaba, T. & Zhang, W. Atomic force microscopy—scanning electrochemical microscopy (AFM-SECM) for nanoscale topographical and electrochemical characterization: principles, applications and perspectives. *Electrochim. Acta* **332**, 135472 (2020).
62. Yu, X. et al. Ten concerns of Zn metal anode for rechargeable aqueous zinc batteries. *Joule* **7**, 1145–1175 (2023).
63. Zhang, X. et al. Single [0001]-oriented zinc metal anode enables sustainable zinc batteries. *Nat. Commun.* **15**, 2735 (2024).
64. Yang, X. et al. Crystallographic manipulation strategies toward reversible Zn anode with orientational deposition. *Adv. Energy Mater.* **14**, 2401293 (2024).
65. Cai, Z. et al. Ultrafast metal electrodeposition revealed by in situ optical imaging and theoretical modeling towards fast-charging Zn battery chemistry. *Angew. Chem. Int. Ed.* **61**, e202116560 (2022).
66. Zheng, Z. et al. An extended substrate screening strategy enabling a low lattice mismatch for highly reversible zinc anodes. *Nat. Commun.* **15**, 753 (2024).
67. Ye, X. P., Celis, J. P., Debonte, M. & Roos, J. R. Ductility and crystallographic structure of zinc foils electrodeposited from acid zinc-sulfate solutions. *J. Electrochem Soc.* **141**, 2698–2708 (1994).
68. Du, W., Yan, J., Cao, C. & Li, C. C. Electrocrystallization orientation regulation of zinc metal anodes: strategies and challenges. *Energy Storage Mater.* **52**, 329–354 (2022).
69. Xing, Z. et al. Facing the capacity fading of vanadium-based zinc-ion batteries. *Trends Chem.* **5**, 380–392 (2023).
70. Zhu, K., Wu, T. & Huang, K. Understanding the dissolution and phase transformation mechanisms in aqueous Zn/α-V₂O₅ batteries. *Chem. Mater.* **33**, 4089–4098 (2021).
71. Kim, Y. et al. Corrosion as the origin of limited lifetime of vanadium oxide-based aqueous zinc ion batteries. *Nat. Commun.* **13**, 2371 (2022).
72. Kang, Y. et al. A Janus separator based on cation exchange resin and Fe nanoparticles-decorated single-wall carbon nanotubes with

- triply synergistic effects for high-areal capacity Zn-I₂ batteries. *Angew. Chem. Int. Ed.* **62**, e202300418 (2023).
73. Chen, G. et al. Toward forty thousand-cycle aqueous zinc-iodine battery: simultaneously inhibiting polyiodides shuttle and stabilizing zinc anode through a suspension electrolyte. *Adv. Funct. Mater.* **33**, 2300656 (2023).
74. Yang, J. L. et al. Hetero-polyionic hydrogels enable dendrites-free aqueous Zn-I₂ batteries with fast kinetics. *Adv. Mater.* **35**, 2306531 (2023).
75. Bale, C. W. et al. Reprint of: FactSage thermochemical software and databases, 2010–2016. *Calphad* **55**, 1–19 (2016).
76. Kresse, G. & Furthmüller, J. Efficient iterative schemes for ab initio total-energy calculations using a plane-wave basis set. *Phys. Rev. B* **54**, 11169–11186 (1996).
77. Blöchl, P. E. Projector augmented-wave method. *Phys. Rev. B* **50**, 17953 (1994).
78. John, P., Perdew, K. B. & Ernzerhof, M. Generalized gradient approximation made simple. *Phys. Rev. Lett.* **77**, 3865 (1996).

Acknowledgements

National Natural Science Foundation of China (No. 22379125, 22109030) [Y. Yang], National Natural Science Foundation of China (22021001) [J.B. Zhao], Fundamental Research Funds for the Central Universities (20720220073) [Y. Yang], The Key Research and Development Program of Yunnan Province (202103AA080019) [J.B. Zhao], Fujian Industrial Technology Development and Application Plan (2022I0002) [Y. Yang]. The authors acknowledge Yonglin Tang and Prof. Yu Qiao from Xiamen University for their help in XAFS testing and analyses. The authors acknowledge Wenhao Yang and Prof. Xue Li from Kunming University of Science and Technology for the DEMS tests. The authors acknowledge Ms. L.W. Lin in Xiamen Legang Materials Technology Co. Ltd for the pH UME and Tan Kah Kee Innovation Laboratory for the help of scientific tests. The numerical calculations in this paper have been done at Hefei advanced computing center. This research employed the resources of the Shanghai Synchrotron Radiation Facility (SSRF) BL11B beamline stations.

Author contributions

M.H. Zhang and Y. Yang conceived and designed the investigation. M.H. Zhang conducted the material and electrochemical tests, analyzed the data, and wrote the manuscript. C.X. Sun and Y.H. Kang performed the DFT calculation. G.H. Chen, Z.H. Lv, J. Yang, S.Y. Li, P.X. Lin, and R. Tang assisted with interpretation of results. Z.P. Wen, and C.C. Li provided

valuable advice on data analysis. J.B. Zhao and Y. Yang supervised and guided the project, and revised the manuscript. All authors discussed the results and commented on the manuscript.

Competing interests

The authors declare no competing interests.

Additional information

Supplementary information The online version contains supplementary material available at <https://doi.org/10.1038/s41467-024-53831-z>.

Correspondence and requests for materials should be addressed to Jinbao Zhao or Yang Yang.

Peer review information *Nature Communications* thanks the anonymous reviewers for their contribution to the peer review of this work. A peer review file is available.

Reprints and permissions information is available at <http://www.nature.com/reprints>

Publisher's note Springer Nature remains neutral with regard to jurisdictional claims in published maps and institutional affiliations.

Open Access This article is licensed under a Creative Commons Attribution-NonCommercial-NoDerivatives 4.0 International License, which permits any non-commercial use, sharing, distribution and reproduction in any medium or format, as long as you give appropriate credit to the original author(s) and the source, provide a link to the Creative Commons licence, and indicate if you modified the licensed material. You do not have permission under this licence to share adapted material derived from this article or parts of it. The images or other third party material in this article are included in the article's Creative Commons licence, unless indicated otherwise in a credit line to the material. If material is not included in the article's Creative Commons licence and your intended use is not permitted by statutory regulation or exceeds the permitted use, you will need to obtain permission directly from the copyright holder. To view a copy of this licence, visit <http://creativecommons.org/licenses/by-nc-nd/4.0/>.

© The Author(s) 2024